

Reduced models for ETG transport in the tokamak pedestal

Citation for published version (APA):

Hatch, D. R., Michoski, C., Kuang, D., Chapman-Oplopoiou, B., Curie, M., Halfmoon, M., Hassan, E., Kotschenreuther, M., Mahajan, S. M., Merlo, G., Pueschel, M. J., Walker, J., & Stephens, C. D. (2022). Reduced models for ETG transport in the tokamak pedestal. *Physics of Plasmas*, 29(6), Article 062501. <https://doi.org/10.1063/5.0087403>

DOI:

[10.1063/5.0087403](https://doi.org/10.1063/5.0087403)

Document status and date:

Published: 01/06/2022

Document Version:

Publisher's PDF, also known as Version of Record (includes final page, issue and volume numbers)

Please check the document version of this publication:

- A submitted manuscript is the version of the article upon submission and before peer-review. There can be important differences between the submitted version and the official published version of record. People interested in the research are advised to contact the author for the final version of the publication, or visit the DOI to the publisher's website.
- The final author version and the galley proof are versions of the publication after peer review.
- The final published version features the final layout of the paper including the volume, issue and page numbers.

[Link to publication](#)

General rights

Copyright and moral rights for the publications made accessible in the public portal are retained by the authors and/or other copyright owners and it is a condition of accessing publications that users recognise and abide by the legal requirements associated with these rights.

- Users may download and print one copy of any publication from the public portal for the purpose of private study or research.
- You may not further distribute the material or use it for any profit-making activity or commercial gain
- You may freely distribute the URL identifying the publication in the public portal.

If the publication is distributed under the terms of Article 25fa of the Dutch Copyright Act, indicated by the "Taverne" license above, please follow below link for the End User Agreement:

www.tue.nl/taverne

Take down policy

If you believe that this document breaches copyright please contact us at:

openaccess@tue.nl

providing details and we will investigate your claim.

Reduced models for ETG transport in the tokamak pedestal

Cite as: Phys. Plasmas **29**, 062501 (2022); <https://doi.org/10.1063/5.0087403>

Submitted: 04 February 2022 • Accepted: 05 May 2022 • Published Online: 02 June 2022

 D. R. Hatch,  C. Michoski,  D. Kuang, et al.



View Online



Export Citation



CrossMark

ARTICLES YOU MAY BE INTERESTED IN

[A survey of pedestal magnetic fluctuations using gyrokinetics and a global reduced model for microtearing stability](#)

Physics of Plasmas **29**, 042503 (2022); <https://doi.org/10.1063/5.0084842>

[Equilibrium reconstruction of DIII-D plasmas using predictive modeling of the pressure profile](#)

Physics of Plasmas **29**, 062502 (2022); <https://doi.org/10.1063/5.0078935>

[Ion thermal transport in the H-mode edge transport barrier on DIII-D](#)

Physics of Plasmas **29**, 012506 (2022); <https://doi.org/10.1063/5.0072155>

Physics of Plasmas

Special Topic: Plasma Physics
of the Sun in Honor of Eugene Parker

Submit Today!



Reduced models for ETG transport in the tokamak pedestal

Cite as: Phys. Plasmas **29**, 062501 (2022); doi: [10.1063/5.0087403](https://doi.org/10.1063/5.0087403)

Submitted: 4 February 2022 · Accepted: 5 May 2022 ·

Published Online: 2 June 2022



View Online



Export Citation



CrossMark

D. R. Hatch,^{1,a)} C. Michoski,² D. Kuang,² B. Chapman-Oplopoiou,³ M. Curie,¹ M. Halfmoon,¹ E. Hassan,^{4,5} M. Kotschenreuther,¹ S. M. Mahajan,¹ G. Merlo,² M. J. Pueschel,^{6,7} J. Walker,¹ and C. D. Stephens¹

AFFILIATIONS

¹Institute for Fusion Studies, University of Texas at Austin, Austin, Texas 78712, USA

²Oden Institute for Computational Engineering and Sciences, University of Texas at Austin, Austin, Texas 78712, USA

³UKAEA-CCFE, Culham Science Centre, Abingdon OX143DB, United Kingdom

⁴Oak Ridge National Laboratory, Oak Ridge, Tennessee 37830, USA

⁵Physics, Faculty of Science, Ain Shams University, Cairo 11566, Egypt

⁶Dutch Institute for Fundamental Energy Research, 5612 AJ Eindhoven, The Netherlands

⁷Eindhoven University of Technology, 5600 MB Eindhoven, The Netherlands

^{a)}Author to whom correspondence should be addressed: drhatch@austin.utexas.edu

ABSTRACT

This paper reports on the development of reduced models for electron temperature gradient (ETG) driven transport in the pedestal. Model development is enabled by a set of 61 nonlinear gyrokinetic simulations with input parameters taken from pedestals in a broad range of experimental scenarios. The simulation data have been consolidated in a new database for gyrokinetic simulation data, the multiscale gyrokinetic database (MGKDB), facilitating the analysis. The modeling approach may be considered a generalization of the standard quasilinear mixing length procedure. The parameter η , the ratio of the density to temperature gradient scale length, emerges as the key parameter for formulating an effective saturation rule. With a single order-unity fitting coefficient, the model achieves an error of 15%. A similar model for ETG particle flux is also described. We also present simple algebraic expressions for the transport informed by an algorithm for symbolic regression.

Published under an exclusive license by AIP Publishing. <https://doi.org/10.1063/5.0087403>

I. INTRODUCTION

This paper reports on the development of reduced models for electron temperature gradient (ETG) driven transport in the pedestal. Reduced models for pedestal transport may facilitate a more comprehensive predictive capability of pedestal structure. MHD-based models like EPED have predicted pedestal pressure in many parameter regimes.^{1,2} However, they typically require pedestal-top density and separatrix quantities as inputs and cannot predict the pedestal structure in regimes not limited by peeling-ballooning modes.^{3,4} Reduced models for pedestal transport may mitigate these weaknesses and expand the scenarios and operating regimes that can be modeled and predicted. Reduced models will also facilitate rapid analysis of pedestal transport, thus expanding the number of discharges and scenarios for which pedestal transport can be analyzed and paving the way for real-time analysis.

Recent work has elucidated the instabilities that are most likely responsible for transport in the pedestal in the various transport

channels.^{5,6} Notably, the disparity between heat diffusivity and particle diffusivity identified by edge modeling points toward a vigorous electron heat transport mechanism that needs to be accounted for. Two instabilities are likely at play: ETG and microtearing modes (MTMs).^{7–9} Since ETG fluctuations exist at scales that are typically inaccessible to diagnostics, we must rely on theory and simulation to infer their activity. Fortunately, while the smallness of the scale makes them indiscernible to diagnostics, it also makes them more amenable to simulation; the scale separation between ETG scales and background quantities—even in the exceedingly narrow pedestal—is sufficient to justify a local flux-tube approach. There is growing evidence from combined numerical–experimental studies that ETG plays an important role in pedestal transport in many H-mode discharges.^{5–7,10–17}

Pedestal ETG turbulence is distinct from ETG turbulence in the core. The extreme density and temperature gradients in the pedestal far surpass those of the background magnetic field, thus circumventing

the typical magnetic drift resonances and favoring slab resonances (for an exception to this claim, see Refs. 10 and 18, which identified toroidal ETG modes destabilized at large radial wavenumbers). This results in turbulence (1) that is isotropic in comparison with the streamer-dominated core ETG,^{19–21} (2) exhibits a high- k_z structure, which demands extreme resolution in the parallel direction, and (3) has contributions from a high number (10–20) of unstable eigenmodes at each wavenumber. Properties (2) and (3) challenge some of the standard approaches to reduce quasilinear modeling, making the present work challenging and timely.

In this paper, we exploit a newly created database for gyrokinetic simulation data—the multiscale gyrokinetic database (MGKDB)—in order to formulate reduced models for pedestal transport from ETG turbulence.

The simulations of which this database is comprised were performed with the GENE gyrokinetic code¹⁹ applied to multiple radial locations in the pedestal for discharges spanning multiple devices (DIII-D, JET, C-Mod, AUG) and operating scenarios. Most of the simulations have been previously described in at least one of Refs. 5–7, 12–16, and 22.

We pursue two general approaches to reduced modeling. First, we investigate variations on the standard quasilinear mixing length approach, wherein a turbulent diffusivity is approximated with step size determined by the perpendicular wavelength of the eigenmode and step time by the linear growth rate. Our modest variation entails allowing for additional parameter dependences in the saturation rule, which are guided by the dataset of nonlinear simulations. Second, we formulate simple algebraic expressions for the transport using a symbolic regression algorithm. In both approaches, the parameter $\eta = L_n/L_{Te}$, the ratio of the density to temperature gradient scale length, emerges as the key parameter. This is consistent with recent theoretical^{13,14} and experimental²³ studies identifying the importance of this parameter for the JET pedestal.

This paper is outlined as follows: The MGKDB database and the dataset are described in Sec. II. The reduced model based on a quasilinear mixing length estimate is described in Sec. III. Various analytic models are described in Sec. IV. Summary and conclusions are found in Sec. V.

II. MGKDB AND THE DATA SET

The dataset consists of 61 nonlinear single-scale ETG simulations. The main parameters for these simulations are shown in the table in the Appendix. The data are shown visually in Fig. 1, which plots the gyroBohm-normalized nonlinear heat flux. Here, the gyroBohm heat flux is defined as $Q_{GB} = n_0 T_0 c_s \frac{\rho_s^2}{a^2}$, where $\rho_s = c_s/\Omega_i$ is the sound gyro-radius, $c_s = \sqrt{T_{0e}/m_i}$ is the sound speed, $\Omega_i = eB_0/m_i$ is the ion gyro-frequency, B_0 is the magnetic field on axis, n_{0e} , T_{0e} are the background electron density and temperature, and a is the minor radius. The parameter $\langle k_y \rangle$ is the spectrally weighted (using the heat flux spectrum) value of k_y , i.e., a value of k_y that is representative of the nonlinearly saturated turbulence and not an input parameter. Most of these simulations were carried out while studying actual discharges on JET, DIII-D, AUG, and C-Mod. Many of the simulations are scans across radial positions in the pedestal or variations of background gradients within error bars. Most of the simulations are described in the following recent publications: Refs. 5–7, 12–16, and 22.

All simulations were uploaded to the MGK database (MGKDB), which was exploited for the analysis in this work. MGKDB is a

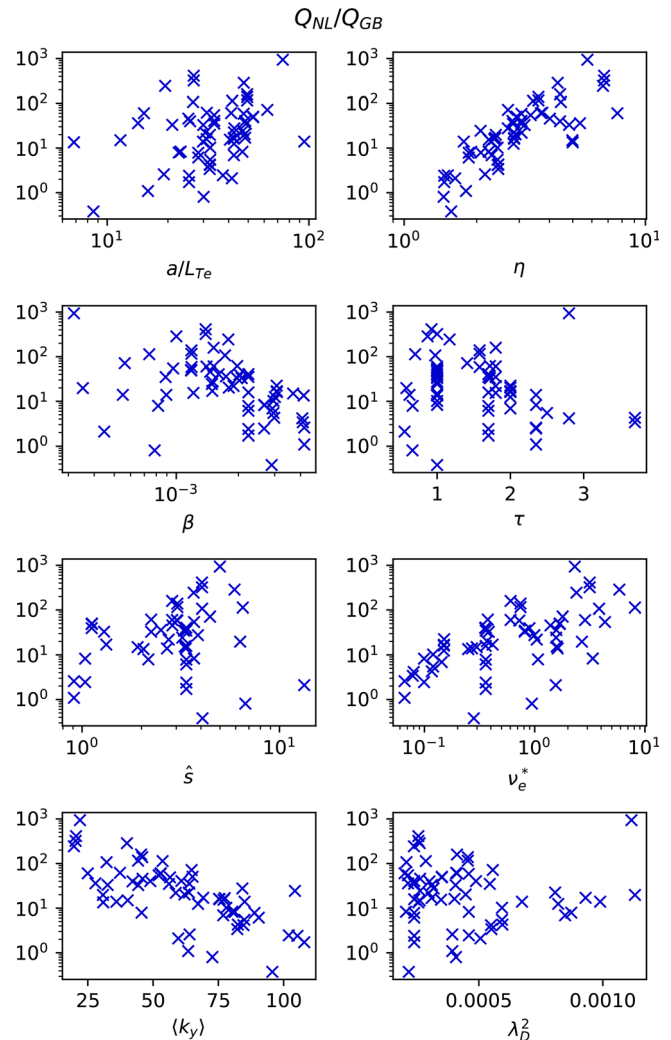


FIG. 1. GyroBohm-normalized heat flux from nonlinear simulations in the data set plotted against several parameters. This data set is used to formulate and test the reduced models in this paper. All parameters are simulation inputs except $\langle k_y \rangle$, which represents the peak wavenumber of the nonlinear heat flux spectrum as defined in the text.

community resource for storing and analyzing gyrokinetic and reduced model simulations. It utilizes a non-relational MongoDB²⁴ (NoSQL) based structure to maximize flexibility so that any output format from any particular code infrastructure can be easily supported. In addition, MGKDB seeks compatibility with an international integrated modeling and analysis suite (IMAS) data standard²⁵ to containerize its quantities of interest and interfaces these data types with a comprehensive Python library called the ordered multidimensional array structures (OMAS) library²⁶ that allows for easy conversion to other data formats including, for example, SQL-based formats. MGKDB may be accessed remotely through either python scripts, command shell options (i.e., MongoDB or Python), a custom graphical user interface, or existing MongoDB graphical user interfaces (GUIs).

Many (but not all) of the simulations were subjected to extensive convergence tests. Generally, for a given study, convergence tests were carried out for a base case, and subsequent scans retained the nominal parameter setup. All simulations were examined to ensure the following: (1) saturated heat fluxes and (2) well-behaved (heat flux peaking much higher than the minimum wavenumber and substantial falloff at high k) heat flux spectra in the perpendicular wavenumbers.

Forty-eight of the simulations employ an adiabatic ion approximation and, thus, dynamically evolve only the electron species. The inclusion of kinetic ions generally does not produce qualitative differences in the heat flux. (Ion dynamics are strongly suppressed by finite Larmor radius (FLR) effects at these electron scales.)^{7,12,13} Six simulations include both ions and electrons, and seven more simulations include three species (including a dynamic impurity). The main transport channel for ETG modes is electron heat. Particle transport is enforced to be zero for simulations with adiabatic ions. Even with kinetic ions, particle transport is generally weak due to FLR suppression of kinetic ion dynamics, which in turn suppresses the particle flux via ambipolarity. Nonetheless, edge modeling indicates that particle diffusivities are generally much smaller than heat diffusivities in the pedestal, so even low levels of the ETG particle flux may be relevant.⁶ Consequently, we use 13 kinetic-ion simulations to generalize the model to include the particle flux.

As is common for simulation studies, some potentially important effects have been neglected. Most notably, we have not accounted for potential multiscale effects. Reference 27 identified, for an idealized setup targeting pedestal-relevant parameters, a reduction of ETG transport due to the interaction with ion-scale microtearing turbulence (or, rather, zonal flows stimulated by it). There is also a possibility of multiscale interaction between different branches of ETG: slab ($k_y \rho_s \sim 100$) and toroidal¹⁸ ($k_y \rho_s \sim 10$). Although a rigorous survey of multiscale effects lies beyond the scope of this work, some simulations were spot-checked with the goal of probing the effects of toroidal ETG modes. For these cases, we did not identify large heat fluxes from toroidal ETG modes nor did interaction with toroidal ETG modes significantly alter the transport levels from slab ETG modes. However, we acknowledge the possibility that such dynamics may play a role for yet-better-resolved and/or longer-simulated runs and/or parameter points that we did not investigate.

We also note that many of the simulations in our dataset produce transport levels in close proximity to the experimental expectations (as noted in previous publications^{5–7,12–16,22}), and none of the simulations significantly exceed experimental transport levels. In short, although uncertainties remain, we consider it very likely that the simulations in this database represent realistic predictions of pedestal ETG transport, and the ETG transport often plays a significant role in the pedestal power balance.

III. GENERALIZED QUASILINEAR MODELS

We first investigate standard quasilinear^{28–31} mixing-length approaches, and generalizations thereof, as illustrated in the following equation:

$$Q_{QL} = a_0(\Theta) \omega_{Te} \text{MAX}_{k_y} \left\{ \frac{\gamma}{\langle k_{\perp}^2 \rangle} \right\}. \quad (1)$$

Here, Q is the electron electrostatic heat flux (gyroBohm normalized as defined above), and $\omega_{Te} = \frac{a}{L_{Te}} = \frac{1}{T_e} \frac{dT_e}{d\rho_{tor}}$ is the normalized inverse

electron temperature gradient scale length. (ρ_{tor} is the square root of the normalized toroidal magnetic flux.) The variable a_0 is a fitting parameter, and $\Theta = (\omega_{Te}, \omega_{ne}, \beta, \hat{s}, \tau, \lambda_D, \nu_e^*)$ simply denotes the possibility of incorporating additional parameter dependences into the saturation rule. Here, β is the ratio of thermal to magnetic energy density, $\tau = \frac{T_e}{T_i} Z_{eff}$, $Z_{eff} = \frac{1}{n_e} \sum_j Z_j^2 n_j$, λ_D is the Debye length, ν_e^* is the normalized electron collision frequency, $\omega_{ne} = \frac{a}{L_{Te}} = \frac{1}{n_e} \frac{dn_e}{d\rho_{tor}}$ is the normalized inverse electron density gradient scale length, and $\hat{s} = \frac{\rho_{tor}}{q} \frac{dq}{d\rho_{tor}}$ is the magnetic shear. These quantities are listed and defined in the Appendix.

A scan over k_y of linear gyrokinetic simulations is used to formulate the mixing length estimate, $\gamma/\langle k_{\perp}^2 \rangle$, where γ is the linear growth rate (normalized to the ratio of the sound speed to minor radius c_s/a) and the eigenmode-averaged perpendicular wavenumber is

$$\langle k_{\perp}^2 \rangle = \frac{\int k_{\perp}^2 |\phi|^2 \kappa(k_{\perp}) dz}{\int |\phi|^2 \kappa(k_{\perp}) dz}. \quad (2)$$

In this equation, z is the distance along the field line, parameterized by the poloidal angle (our standard domain for this problem is $-7\pi < z < 7\pi$; smaller integration ranges were also tested with negligible difference), ϕ is the electrostatic potential for the eigenmode, $k_{\perp}^2 = g_{xx} k_x^2 + 2g_{xy} k_x k_y + g_{yy} k_y^2$ is the perpendicular wavenumber, $k_x(k_y)$ is the radial (binormal) wavenumber, g_{ij} are the relevant components of the metric tensor, and $\kappa(k_{\perp}) = (1 + \frac{2(k_{\perp}^2 + 2/3\pi k_{\perp}^4)}{(1+2/3k_{\perp}^2)})^{-1/2} \approx J_0(k_{\perp})^2$ approximates the Bessel functions that represent gyroaveraging. Note that, due to magnetic shear, the radial wavenumber is connected to the parallel coordinate, z , as follows: $k_x = z \hat{s} k_y$. All wavenumbers are normalized to the sound gyroradius $\frac{m_i c_s}{e B_0}$.

The mixing length $\gamma/\langle k_{\perp}^2 \rangle$ is motivated as a turbulent diffusivity with relevant scale length, $1/k_{\perp}$, and timescale, $1/\gamma$, set by the linear instabilities. We chose the scan range $10 \leq k_y \rho_s \leq 240$. The maximum value of the mixing length diffusivity over the scan is selected for the model. Several variations were considered, and, to some extent, tested, including: (1) scanning also the ballooning angle, (2) maximizing or summing over multiple eigenmodes using the GENE eigenmode solver, (3) summing (as opposed to maximizing) over the k_y scan, and (4) including an additional factor of the ratio of the heat flux to the density fluctuation amplitude $Q/|n|^2$. None of these generalizations substantially improved the model, and some actually reduced accuracy. Consequently, we have retained the simplest, and most computationally inexpensive, approach: limiting the scan to the most unstable eigenmode at zero ballooning angle and maximizing the mixing length over k_y .

A. Heat flux

The assumption of constant a_0 represents the standard mixing length estimate, which has been effective in modeling transport in several scenarios, including Refs. 29, 32, and 33. We test this simplest expression right away and find that it results in substantial errors when attempting to model the transport across the dataset, as shown in Fig. 2.

To quantify the accuracy, we define a modified relative error as

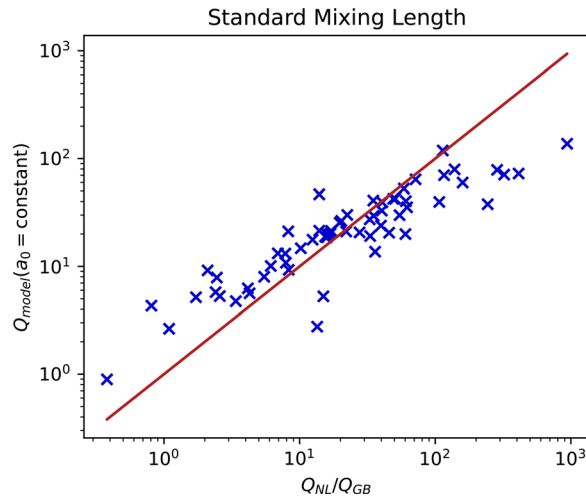


FIG. 2. The standard mixing length estimate (assuming a_0 is constant) (y axis) plotted against the nonlinear simulations result (x axis) for the same parameter point. As with many following figures, the accuracy of the model can be gauged by how closely the points cluster around the line. The error for this model is $\varepsilon = 0.35$.

$$\varepsilon = \sqrt{\frac{1}{N} \sum \frac{(Q_{NL} - Q_{model})^2}{(Q_{model} + Q_{NL})^2}}, \quad (3)$$

which equally penalizes errors in the limits $Q_{model} \ll Q_{NL}$ and $Q_{model} \gg Q_{NL}$ (N is the number of simulations in the dataset). The standard mixing length estimate produces $\varepsilon = 0.35$.

As a next step, we return to the database to investigate additional parameter dependences in $a_0 = \frac{Q_{NL}}{\omega_{Te} \text{MAX}_{ky} \left\{ \frac{\gamma}{(k_{\perp}^2)} \right\}}$, which we define here

as the ratio between the nonlinear heat flux and the mixing length estimate. This is shown in Fig. 3, where one clear correlation immediately appears as $a_0 \propto \eta^2$. We modify this slightly as follows with an eye toward future applications to scenarios with extremely weak density gradients: $\eta = \frac{\omega_{Te}}{\omega_{ne}} \rightarrow \hat{\eta} = \frac{\omega_{Te}}{1 + \omega_{ne}}$. This modification has very little effect within the current dataset, for which ω_n is typically much larger than unity, but ensures well-behaved solutions in the limit $\omega_n \rightarrow 0$. We, thus, arrive at the model that constitutes the core result of this paper,

$$Q_{QL} = 0.87 \hat{\eta}^2 \omega_{Te} \text{MAX}_{ky} \left\{ \frac{\gamma}{(k_{\perp}^2)} \right\}, \quad (4)$$

which is shown in Fig. 4.

As can be seen in Fig. 4, with few exceptions, the model accurately recovers the nonlinear heat flux across the dataset. The error for the model defined in Eq. (4) is $\varepsilon = 0.15$. (Recall that the error for the standard quasilinear model is $\varepsilon = 0.35$.) We, thus, have arrived at a model based on a physical (gyrokinetic) quasilinear mixing-length estimate, one additional parameter dependence (η^2), and a single order-unity fitting parameter that effectively reproduces heat fluxes from a large dataset of nonlinear gyrokinetic simulations.

While a thorough investigation of the origin of the additional η dependence is beyond the scope of this work, we will make a few simple observations. Figure 5 shows the inverse of the spectrally averaged k_y , plotted against η , demonstrating a clear proportionality between the

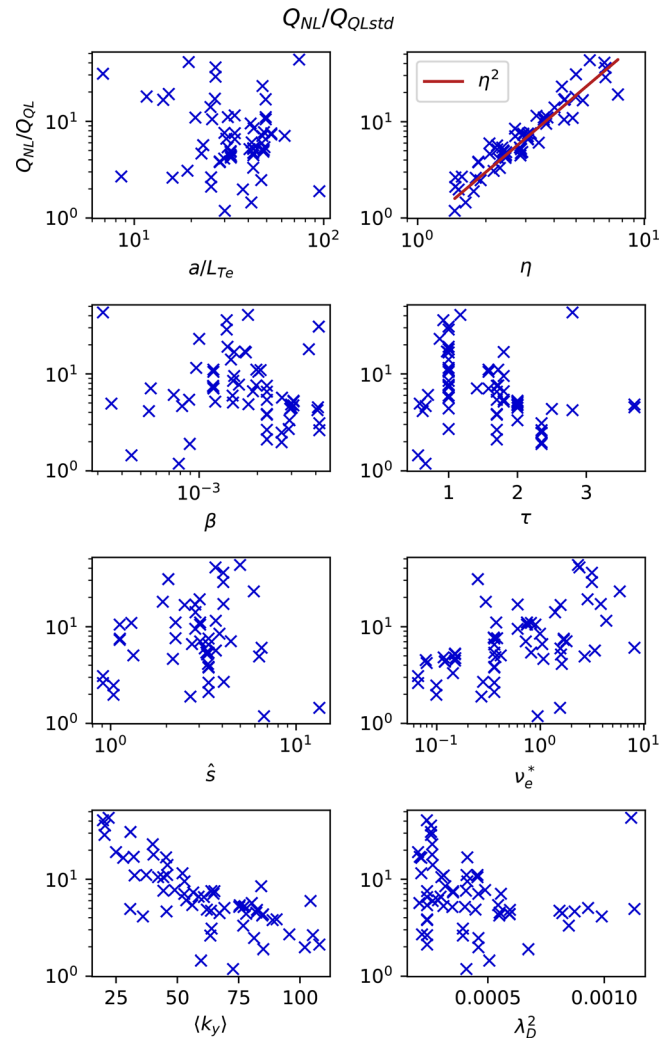


FIG. 3. The ratio of the heat flux to the standard mixing length estimate is plotted against the parameters in order to identify additional relevant parameter dependences for the saturation rule. A clear correlation with η^2 is identified as shown by the line.

two. The nonlinear spectrum condenses at lower wavenumbers as η increases, thus enhancing the transport. There is some evidence in the dataset that this downshift exceeds that predicted by the mixing-length estimate, thus requiring the additional factor of η^2 to compensate. A deeper understanding of the η^2 dependence will be pursued in the future work.

B. Particle flux

In this section, we investigate similar reduced models for particle transport from pedestal ETG. The particle flux from ETG modes is very modest; the ambipolar (net zero radial charge flux) nature of gyrokinetic transport means that electron particle transport is constrained to small levels by the low ion particle transport due to FLR effects on the ions. However, the pedestal parameter regime of interest

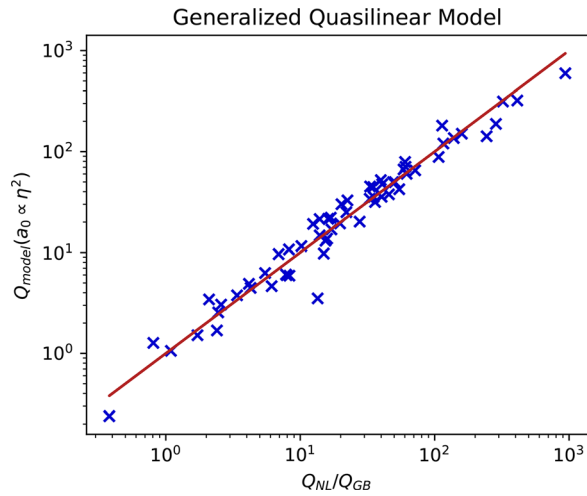


FIG. 4. The quasilinear model defined in Eq. (4) is quite accurate ($\varepsilon = 0.15$) and represents the major result of this work.

is also characterized by low particle transport; several studies have demonstrated via edge modeling that electron heat diffusivity greatly surpasses electron particle diffusivity in the pedestal:^{6,34} $D_e/\chi_e \ll 1$. Gyrokinetic simulations have demonstrated that, while ETG particle transport is not likely to account for the bulk of the transport, it is often at levels that are not negligible.⁶ Moreover, gyrokinetic simulations often exhibit particle pinches,⁶ which could be important for fueling the pedestal beyond the capacity of neutral penetration alone.

Thirteen simulations in the dataset retain kinetic ions (seven of those including also an impurity species). Kinetic ions also open the possibility of additional instabilities in the lower wavenumber ranges, but such instabilities have not been observed in these scenarios for the wavenumber ranges of interest. The electron particle flux for these simulations is shown in Fig. 6 (normalized to $\Gamma_{GB} = \frac{n_0 \rho_i^2 c_s}{a^2}$). Note the

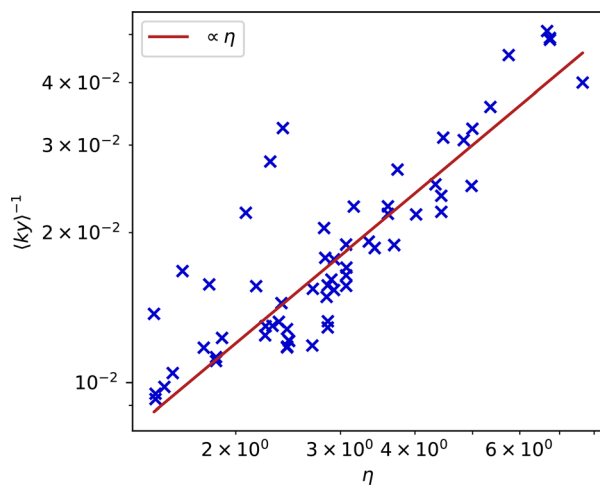


FIG. 5. The inverse of the spectrally averaged wavenumber $\langle k_y \rangle^{-1}$ plotted against η .

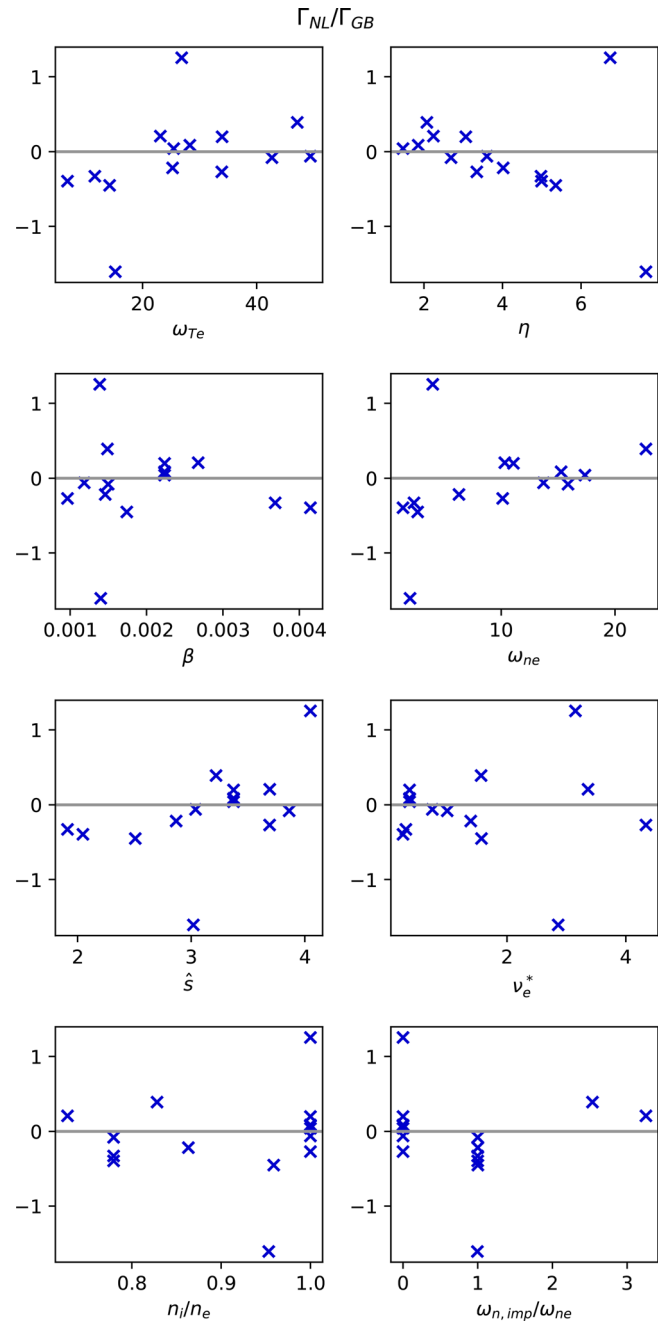


FIG. 6. The gyroBohm-normalized particle flux plotted against several parameters.

existence of both positive and negative fluxes in the dataset and the density gradient ω_n roughly parameterizes the transition between the two signs. Two simulations (at high η) exhibit particle fluxes of order unity: one positive and one negative. The simulation with a large positive particle flux is particularly anomalous; it has a relatively low density gradient, and most of its defining parameters are quite similar to the simulation with a large negative particle flux.

Perhaps, the most obvious generalization of the model to include the particle flux would weight the heat flux prediction [Eq. (4)] by the quasilinear ratio of the fluxes as follows:

$$\Gamma_{QL,naive} = Q_{QL} \text{MAX}_{ky} \left\{ \frac{\Gamma_e}{Q_e} \right\}, \quad (5)$$

where Q_{QL} is the model defined above for the heat flux [defined in Eq. (4)] and the final term denotes the maximum of the ratio of the particle to heat flux defined by the linear modes maximized over the k_y scan. As shown in Fig. 7, this model is not very accurate under predicting, in particular, the extreme flux cases. We find that one additional factor of η improves the model substantially:

$$\Gamma_{QL} = \hat{\eta} Q_{QL} \text{MAX}_{ky} \left\{ \frac{\Gamma_e}{Q_e} \right\}. \quad (6)$$

Note that this model includes one *additional* factor of η beyond those already included in Q_{QL} . As seen in Fig. 7, this improves the agreement significantly, particularly for the cases with large fluxes. Notably, this model reproduces the transition between positive and negative fluxes

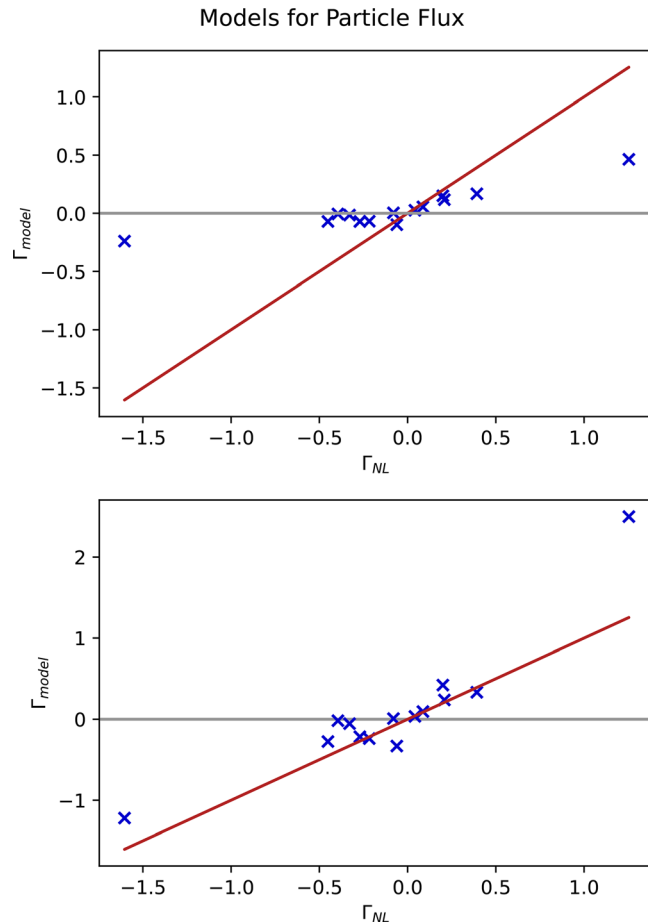


FIG. 7. The models $\Gamma_{QL,naive} = Q_{QL} \text{MAX}_{ky} \left\{ \frac{\Gamma_e}{Q_e} \right\}$ [Eq. (5)] (top) and $\Gamma_{QL} = \hat{\eta} Q_{QL} \text{MAX}_{ky} \left\{ \frac{\Gamma_e}{Q_e} \right\}$ [Eq. (6)] (bottom). Note that Eq. (6) successfully reproduces the sign of the particle flux for nearly all (one exception) simulations.

and distinguishes between the two simulations with large fluxes (one positive and one negative) despite their apparent proximity in parameter space.

IV. ALGEBRAIC EXPRESSIONS

Although we have formulated a rather accurate quasilinear model for pedestal transport, this model still requires several linear gyrokinetic simulations. This represents enormous savings in comparison with full nonlinear simulations, but a simple algebraic expression would still be desirable for the purpose of rapid evaluation and physical intuition. Consequently, as a final investigation, we abandon the quasilinear mixing-length framework entirely and investigate simple algebraic expressions for the fluxes.

To this end, we apply a novel symbolic regression algorithm, which minimizes the error by systematically surveying combinations of pre-selected algebraic forms. More specifically, the algorithm, called system identification and regression (SIR), minimizes Eq. (7) relative to a collection of rational functions of fixed top admissible monomial degree d (in its elements), fixed top admissible nonlinearity order n_ℓ per input (in its elements), and a maximum number of linearly combined terms n_u allowed in the resulting expression (in either the numerator or the denominator). For example,

$$\text{MIN}_{a,b} \varepsilon \left(y, \frac{a_1 \mathbf{P}_1(\mathbf{u}) + \dots + a_m \mathbf{P}_m(\mathbf{u})}{b_1 \mathbf{Q}_1(\mathbf{u}) + \dots + b_n \mathbf{Q}_n(\mathbf{u})} \right), \quad (7)$$

where y is the target, \mathbf{u} are the inputs, and a_i and b_i are the coefficients on the monomial numerator \mathbf{P}_i and denominator \mathbf{Q}_i terms. The resulting ε is then computed and stored at each degree $d_0 \in [0, d]$ consecutively for all admissible nonlinear combinations starting at $n_u = 1$ and results in an ordered set of candidate rational function expressions effectively minimizing ε . These candidate expressions are then surveyed, and the most likely resultant expression is chosen based on physics insight.

In carrying out this exercise, we are wary of over-fitting, particularly for the small set of particle flux data. Consequently, we favor simple expressions with willingness to sacrifice to some extent accuracy.

Figure 8 shows four models defined in the following equations [corresponding to (a)–(d), respectively]. The models are defined below and summarized in Table I:

$$Q_1 = \sqrt{\frac{m_e}{m_i}} \omega_{Te} (a_0 + b_0 \eta^2), \quad (8)$$

where $a_0 = -12.1$ and $b_0 = 6.73$ with error $\varepsilon = 0.290$,

$$Q_2 = \sqrt{\frac{m_e}{m_i}} \omega_{Te} (a_0 + b_0 \eta^4), \quad (9)$$

where $a_0 = 1.44$ and $b_0 = 0.50$ with error $\varepsilon = 0.279$,

$$Q_3 = \sqrt{\frac{m_e}{m_i}} \omega_{Te} (a_0 + b_0 \eta^4 / \tau), \quad (10)$$

where $a_0 = 3.23$ and $b_0 = 0.63$ with error $\varepsilon = 0.303$,

$$Q_4 = \sqrt{\frac{m_e}{m_i}} \omega_{Te}^2 (a_0 + b_0 \eta), \quad (11)$$

where $a_0 = -1.26$ and $b_0 = 0.919$ with error $\varepsilon = 0.368$.

Analytic Models

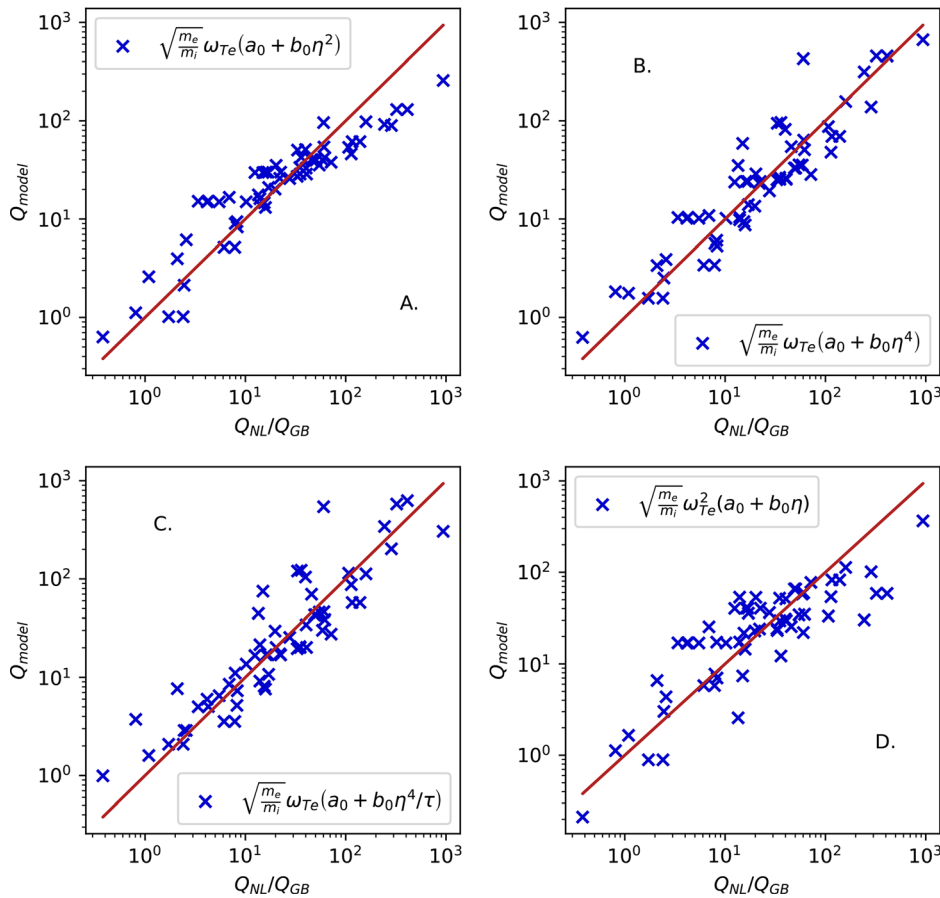


FIG. 8. The models defined in Eqs. (8)–(11) are plotted in (a)–(d), respectively.

The final expression follows the form proposed in Ref. 17. This does indeed qualitatively capture the major trend of the data but is not as accurate for this dataset as Eqs. (8)–(10). We view Eqs. (9) and (10) as likely the most reliable. Equation (9) captures the major trends

TABLE I. Summary of algebraic expressions [defined in Eqs. (8)–(12)] for the heat flux along with errors.

Model	a_0	b_0	ϵ
$Q_1 = \sqrt{\frac{m_e}{m_i}} \omega_{Te} (a_0 + b_0 \eta^2)$	−12	6.7	0.29
$Q_2 = \sqrt{\frac{m_e}{m_i}} \omega_{Te} (a_0 + b_0 \eta^4)$	1.4	0.5	0.28
$Q_3 = \sqrt{\frac{m_e}{m_i}} \omega_{Te} (a_0 + b_0 \eta^4 / \tau)$	3.2	0.63	0.30
$Q_4 = \sqrt{\frac{m_e}{m_i}} \omega_{Te}^2 (a_0 + b_0 \eta)$	−1.3	0.92	0.37
$Q_5 = \sqrt{\frac{m_e}{m_i}} a_0 \omega_{Te} (b_0 + \eta)^4$	0.31	0.41	0.27

using only simple combinations of the gradients. Equation (10) additionally incorporates a factor of $\tau = \frac{T_e}{T_i} Z_{eff}$. Note that τ is only relevant for simulations with adiabatic ions; it captures the effects of the ions in the field equation and is well known to be stabilizing.

Many similar expressions produce similar accuracy. For example, in the following expression, the model applies the exponent outside the parentheses in a form that would reflect threshold behavior more transparently:

$$Q_5 = \sqrt{\frac{m_e}{m_i}} a_0 \omega_{Te} (b_0 + \eta)^4, \quad (12)$$

where $a_0 = 0.309$, $b_0 = 0.413$, and error $\epsilon = 0.271$. The result is very similar to that in Eq. (10). Slight differences like these, however, may become important when attempting to capture the transport near threshold.

Although we have used a very simple gyroBohm normalization (defined above), the more-natural variation for ETG transport would be^{12,17} $Q_{eGB} = n_{e0} T_{e0} v_{Te} \frac{\rho_s^2}{L_{Te}^2}$, where L_{Te} is the electron temperature gradient scale length. If this is interpreted in terms of Fick's law $Q = n \nabla T \chi$, then one factor of $1/L_{Te}$ comes from the gradient and the other comes from the assumption that the ETG growth rate scales like

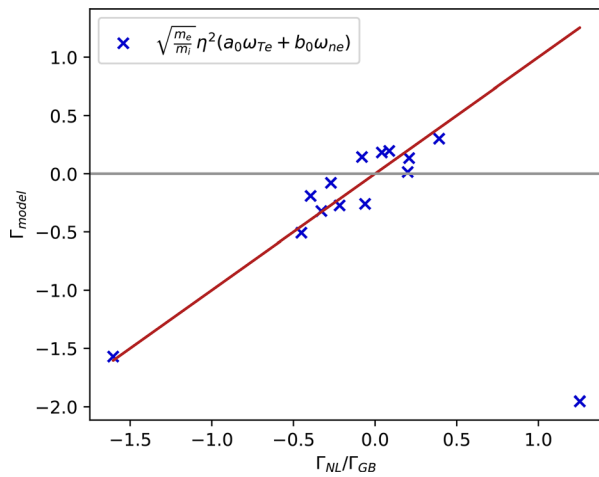


FIG. 9. The model defined in Eq. (13). Note the outlier in the lower right corner of the figure.

v_{Te}/L_{Te} . However, for slab ETG, the growth rate is dependent on $\eta = L_n/L_T$ as opposed to L_{Te} alone. This may explain the superior fit in Eqs. (8)–(10) (which entail a single factor of ω_{Te}) in comparison with Eq. (11) (with ω_{Te}^2).

We also note that Ref. 35 proposes a model for ETG transport with very strong dependence on gradient scale lengths $Q_e \propto \omega_{Te}^5$ similar to Eqs. (9) and (10). However, in contrast to our expressions, the model includes not only temperature gradients but also density gradients (i.e., it is not parameterized in terms of η and does not capture the stabilizing effects of density gradients). This may be attributable to its focus on a core-like parameter regime, where curvature-driven (as opposed to slab) ETG is salient.

For particle transport, we propose an expression that includes a diffusive and pinch component, amplified by η^2 as shown in Fig. 9 and defined in the following equation:

$$\Gamma_1 = \sqrt{\frac{m_e}{m_i}} \eta^2 (a_0 \omega_{Te} + b_0 \omega_{ne}), \quad (13)$$

where $a_0 = -0.18$ and $b_0 = 0.56$. Note that these expressions (as well as all others we investigated) are not capable of capturing the simulation with large positive particle flux in contrast with the quasilinear model defined above in Eq. (6). It is likely that a more sophisticated treatment of geometry and/or impurities would be necessary to achieve a more comprehensive expression for the particle flux.

V. SUMMARY AND CONCLUSIONS

This paper has presented reduced models for ETG transport in the pedestal. The development of the models exploited a dataset of 61 nonlinear simulations from the MGKDB database. As may be expected for slab ETG modes, the parameter η emerges as the key parameter for both the quasilinear mixing-length approach as well as simple algebraic expressions for the transport. The most important models are reproduced here for easy reference.

The best quasilinear mixing length model for the heat flux identified in this work [$\hat{\eta} = \omega_{Te}/(1 + \omega_{ne})$] is

$$Q_{QL} = 0.867 \hat{\eta}^2 \omega_{Te} \text{MAX}_{ky} \left\{ \frac{\gamma}{\langle k_{\perp}^2 \rangle} \right\}. \quad (14)$$

The best quasilinear mixing length model for the particle flux is identified in this work:

$$\Gamma_{QL} = \hat{\eta} Q_{QL} \text{MAX}_{ky} \left\{ \frac{\Gamma_e}{Q_e} \right\}, \quad (15)$$

where Q_{QL} is defined immediately above.

The best algebraic expression for the heat flux identified in this work is (un-normalized with quantities defined in Sec. II),

$$Q_3 = \left[\sqrt{\frac{m_e}{m_i}} n_{0e} T_{0e} c_s \frac{\rho_s^2}{a^2} \right] \omega_{Te} (3.23 + 0.63 \eta^4 / \tau) \quad (16)$$

or

$$Q_2 = \left[\sqrt{\frac{m_e}{m_i}} n_{0e} T_{0e} c_s \frac{\rho_s^2}{a^2} \right] \omega_{Te} (1.44 + 0.5 \eta^4). \quad (17)$$

Slight variations to these expressions, for example, applying the exponent outside of the parentheses $[(a_0 + \eta)^4]$ may be useful to explore closer to the stability threshold.

The best algebraic expression for the particle flux identified in this work is (un-normalized),

$$\Gamma_1 = \left[\sqrt{\frac{m_e}{m_i}} n_{0e} c_s \frac{\rho_s^2}{a^2} \right] \eta^2 (-0.18 \omega_{Te} + 0.56 \omega_{ne}). \quad (18)$$

Further refinements may be expected as additional scenarios are explored. For example, additional simulation data near threshold or at the pedestal top would be informative. Moreover, an open question is to what extent the current dataset (and the currently explored experimental space) represents the next generation of devices. We make two speculative comments in this context. First, the ITER-like wall (ILW) on JET has produced pedestal behavior distinct from carbon wall JET operation.^{13,14} Increased gas puffing was required to mitigate tungsten sputtering, which translated into higher separatrix density, an outward-shifted density pedestal, and higher η . It remains an open question how these considerations will extrapolate to ITER, where divertor constraints will be even more stringent. Second, the neutral opacity will be strongly decreased for ITER,³⁶ raising the question of how this will affect the formation and structure of the density pedestal.

Several applications of these models are envisioned, including: (1) rapid analysis of experimental discharges and (2) a component of more comprehensive models for the pedestal structure.

ACKNOWLEDGMENTS

We would like to thank several collaborators in the Partnership for Multiscale Gyrokinetic Turbulence (MGK) and Anthony Field for useful discussions. This research used resources of the National Energy Research Scientific Computing Center, a DOE Office of Science User Facility, and the Texas Advanced Computing Center (TACC) at The University of Texas at Austin. This work was supported by U.S. DOE under Contract No. DE-FG02-04ER54742, and the U.S. DOE Office of Fusion Energy Sciences Scientific Discovery through Advanced Computing

(SciDAC) program under Award No. DE-SC0018429. This work has been carried out within the framework of the EUROfusion Consortium, funded by the European Union via the Euratom Research and Training Programme (Grant Agreement No. 101052200 EUROfusion). Views and opinions expressed are, however, those of the author(s) only and do not necessarily reflect those of the European Union or the European Commission. Neither the European Union nor the European Commission can be held responsible for them.

AUTHOR DECLARATIONS

Conflict of Interest

The authors have no conflicts to disclose.

DATA AVAILABILITY

The data that support the findings of this study are available from the corresponding author upon reasonable request.

APPENDIX: DATA SET

The parameters in Table II are $\omega_{Te} = \frac{a}{L_{Te}} = 1/T_e d\rho_{tor}/dT_e$, $\omega_{ne} = \frac{a}{L_{ne}} = 1/n_e d\rho_{tor}/dn_e$, $\eta = \omega_{Te}/\omega_{ne}$, $\tau = \frac{T_{e0}}{T_{i0}} Z_{eff}$, the ratio of thermal to magnetic energy $\beta = 8\pi n_{e0} T_{e0}/B_0^2$ (cgs), magnetic shear $\hat{s} = \frac{\rho_{tor}}{q} \frac{dq}{d\rho_{tor}}$, the Debye length normalized to the sound gyroradius λ_D/ρ_s , and the normalized electron collision frequency $\nu_e^* = \frac{16}{3\sqrt{\pi}} \frac{qZ^2}{e^{3/2}} \frac{R}{a} \frac{n_i}{n_e} \frac{\pi \ln(\Lambda)}{2^{3/2} T_{e0}^2}$. These are standard GENE definitions, which can be found in the GENE documentation [genecode.org].

TABLE II. Table of the main parameters along with the gyroBohm-normalized heat flux (final column) for the 61 nonlinear simulations analyzed in the paper.

Case	ω_{Te}	ω_{ne}	η	τ	\hat{s}	β	ν_{*e}	λ_D^2	ρ_{tor}	Spec.	Q_e/Q_{GB}
1	26.7	5.97	4.46	0.975	4.06	0.001 72	3.84	0.000 208	0.97	1	107.0
2	31.2	8.34	3.74	1.72	2.24	0.001 97	0.375	0.000 409	0.965	1	61.9
3	49.4	13.7	3.6	1.58	3.04	0.001 18	0.743	0.000 455	0.975	1	116.0
4	19.4	2.91	6.67	1.17	3.68	0.001 79	2.39	0.000 238	0.97	1	244.0
5	47.6	11.0	4.33	0.87	5.92	0.001	5.85	0.000 261	0.985	1	286.0
6	26.9	3.98	6.74	0.923	4.05	0.001 39	3.15	0.000 256	0.97	1	412.0
7	41.7	12.2	3.42	0.7	6.52	0.000 74	8.11	0.000 286	0.985	1	114.0
8	94.8	53.7	1.77	2.35	2.69	0.000 895	0.27	0.000 674	0.985	1	14.0
9	21.0	4.35	4.83	1	1.29	0.002 08	0.812	0.000 311	0.9675	1	33.1
10	52.9	18.1	2.93	1	1.12	0.001 18	1.68	0.000 351	0.98	1	49.0
11	74.2	12.9	5.75	2.8	4.99	0.000 319	2.31	0.001 12	0.5	1	938.0
12	19.1	8.83	2.16	2.35	0.909	0.004 17	0.0661	0.000 393	0.965	1	2.58
13	48.7	17.2	2.83	1.8	3.28	0.000 888	0.816	0.000 544	0.975	1	34.9
14	8.55	5.45	1.57	1	4.07	0.002 9	0.28	0.000 217	0.965	1	0.38
15	32.2	13.1	2.46	3.7	-2.19	0.002 99	0.117	0.000 595	0.9675	1	4.28
16	30.1	20.6	1.46	0.664	6.72	0.000 785	0.942	0.000 408	0.972	1	0.807
17	41.5	25.5	1.63	0.556	13.4	0.000 448	1.55	0.000 506	0.982	1	2.1
18	22.6	10.9	2.08	0.666	2.17	0.000 817	1.07	0.000 873	0.962	1	7.92
19	29.8	13.1	2.29	0.623	3.35	0.000 551	1.61	0.000 989	0.972	1	14.0
20	32.3	13.5	2.4	0.581	6.32	0.000 353	2.68	0.001 13	0.982	1	19.8
21	25.5	17.4	1.47	1.7	3.37	0.002 24	0.36	0.000 239	0.975	1	1.72
22	28.3	15.3	1.85	1.7	3.37	0.002 24	0.36	0.000 239	0.975	1	6.13
23	31.1	13.2	2.36	1.7	3.37	0.002 24	0.36	0.000 239	0.975	1	15.9
24	33.9	11.1	3.07	1.7	3.37	0.002 24	0.36	0.000 239	0.975	1	35.2
25	25.8	5.82	4.43	1	1.12	0.002 02	0.897	0.000 301	0.97	1	39.8
26	52.9	18.1	2.92	1	1.12	0.001 18	1.69	0.000 351	0.98	1	50.5
27	42.5	14.9	2.85	2.0	-0.789	0.003 07	0.151	0.000 808	0.975	1	22.5
28	48.3	20.2	2.39	2.0	1.33	0.001 5	0.415	0.000 93	0.978	1	17.1
29	42.5	15.0	2.84	2.0	-0.715	0.003 01	0.15	0.000 82	0.975	1	12.5
30	42.5	18.4	2.31	2.0	-0.895	0.002 93	0.143	0.000 848	0.975	1	6.91
31	48.0	16.6	2.9	2.0	-0.477	0.001 8	0.369	0.000 447	0.978	1	20.3
32	37.5	24.7	1.52	2.35	1.04	0.002 66	0.0991	0.000 46	0.975	1	2.45

TABLE II. (Continued.)

Case	ω_{Te}	ω_{ne}	η	τ	\hat{s}	β	ν_{*e}	λ_D^2	ρ_{tor}	Spec.	Q_e/Q_{GB}
33	42.5	14.9	2.85	2.0	−0.794	0.003 07	0.15	0.000 309	0.975	1	16.9
34	32.4	13.3	2.44	1	−2.05	0.002 96	0.12	0.000 593	0.9675	1	10.2
35	32.4	13.3	2.44	2.5	−2.05	0.002 96	0.12	0.000 593	0.9675	1	5.48
36	40.6	18.1	2.24	1.8	3.32	0.001 21	1.58	0.000 348	0.975	1	15.4
37	30.6	9.98	3.07	1.8	2.75	0.001 9	1.04	0.000 297	0.97	1	22.0
38	41.2	11.2	3.69	1.8	2.86	0.001 52	0.605	0.000 412	0.97	1	60.7
39	49.4	11.2	4.43	1.8	2.86	0.001 52	0.605	0.000 412	0.97	1	159.0
40	32.3	13.2	2.44	2.8	−2.14	0.004 08	0.08	0.000 549	0.9675	1	4.15
41	32.2	13.1	2.46	3.7	−2.25	0.004 1	0.0784	0.000 551	0.9675	1	3.39
42	42.5	14.9	2.86	2.0	−0.811	0.003 07	0.15	0.000 402	0.975	1	16.1
43	48.4	17.2	2.81	1	−0.014 9	0.001 61	0.355	0.000 488	0.978	1	40.3
44	14.2	2.66	5.36	n/a	2.51	0.001 74	1.57	0.000 214	0.96	3	36.0
45	6.84	1.37	5.0	n/a	2.05	0.004 15	0.249	0.000 256	0.934	3	13.5
46	15.2	1.99	7.65	n/a	3.02	0.001 4	2.86	0.000 2	0.973	3	60.2
47	42.7	15.9	2.69	n/a	3.86	0.001 5	0.993	0.000 317	0.973	3	27.7
48	25.3	6.29	4.02	n/a	2.87	0.001 46	1.39	0.000 263	0.964	3	45.7
49	33.9	10.1	3.35	n/a	3.69	0.000 966	4.34	0.000 214	0.986	2	54.5
50	11.6	2.34	4.98	n/a	1.91	0.003 68	0.298	0.000 261	0.945	3	15.0
51	29.9	9.48	3.16	1.72	2.24	0.001 97	0.383	0.000 406	0.965	1	32.9
52	47.5	15.5	3.06	1.58	3.04	0.001 19	0.725	0.000 459	0.975	1	58.7
53	62.2	23.1	2.69	1.41	4.45	0.000 563	1.79	0.000 556	0.985	1	71.6
54	15.9	8.83	1.8	2.35	0.909	0.004 17	0.0661	0.000 393	0.965	1	1.09
55	46.8	24.7	1.9	2.35	1.04	0.002 66	0.0991	0.000 46	0.975	1	8.24
56	23.1	10.3	2.24	n/a	3.69	0.002 68	3.36	0.000 206	0.5	3	8.31
57	25.5	17.4	1.47	n/a	3.37	0.002 24	0.36	0.000 239	0.975	2	2.4
58	28.3	15.3	1.85	n/a	3.37	0.002 24	0.36	0.000 239	0.975	2	7.84
59	33.9	11.1	3.07	n/a	3.37	0.002 24	0.36	0.000 239	0.975	2	40.7
60	26.9	3.98	6.74	n/a	4.05	0.001 39	3.15	0.000 256	0.97	2	322.0
61	49.4	13.7	3.6	n/a	3.04	0.001 18	0.743	0.000 455	0.975	2	139.0

REFERENCES

- ¹P. B. Snyder, R. J. Groebner, A. W. Leonard, T. H. Osborne, and H. R. Wilson, "Development and validation of a predictive model for the pedestal height," *Phys. Plasmas* **16**, 056118 (2009).
- ²P. B. Snyder, N. Aiba, M. Beurskens, R. J. Groebner, L. D. Horton, A. E. Hubbard, J. W. Hughes, G. T. A. Huysmans, Y. Kamada, A. Kirk, C. Konz, A. W. Leonard, J. Lonnroth, C. F. Maggi, R. Maingi, T. H. Osborne, N. Oyama, A. Pankin, S. Saarelma, G. Saibene, J. L. Terry, H. Urano, and H. R. Wilson, "Pedestal stability comparison and ITER pedestal prediction," *Nucl. Fusion* **49**, 085035 (2009).
- ³S. Saarelma, L. Frassinetti, P. Bilkova, C. D. Challis, A. Chankin, R. Fridström, L. Garzotti, L. Horvath, and C. F. Maggi, "Self-consistent pedestal prediction for JET-ILW in preparation of the DT campaign," *Phys. Plasmas* **26**(7), 072501 (2019).
- ⁴L. Frassinetti, S. Saarelma, G. Verdoolaege, M. Groth, J. C. Hillesheim, P. Bilkova, P. Bohm, M. Dunne, R. Fridström, E. Giovannozzi, F. Imbeaux, B. Labit, E. de la Luna, C. Maggi, M. Owsiak, and R. Scannell, "Pedestal structure, stability and scalings in JET-ILW: The EUROfusion JET-ILW pedestal database," *Nucl. Fusion* **61**(1), 016001 (2020).
- ⁵M. Kotschenreuther, X. Liu, D. R. Hatch, S. Mahajan, L. Zheng, A. Diallo, R. Groebner, DIII-D TEAM, J. C. Hillesheim, C. F. Maggi, C. Giroud, F. Koehl, V. Parail, S. Saarelma, E. Solano, A. Chankin, and JET Contributors, "Gyrokinetic analysis and simulation of pedestals to identify the culprits for energy losses using 'fingerprints,'" *Nucl. Fusion* **59**(9), 096001 (2019).
- ⁶D. R. Hatch, M. T. Kotschenreuther, S. M. Mahajan, M. Halfmoon, E. Hassan, G. Merlo, C. Michoski, J. Canik, A. Sontag, I. Joseph, M. Umansky, W. Guttenfelder, A. Diallo, R. Groebner, A. O. Nelson, F. Laggner, J. Hughes, and S. Mordijck, "Final report for the FY19 FES theory performance target," Report No. 1615233 (2019).
- ⁷D. R. Hatch, M. Kotschenreuther, S. Mahajan, P. Valanju, F. Jenko, D. Told, T. Görler, and S. Saarelma, "Microtearing turbulence limiting the JET-ILW pedestal," *Nucl. Fusion* **56**(10), 104003 (2016).
- ⁸D. R. Hatch, M. Kotschenreuther, S. M. Mahajan, M. J. Pueschel, C. Michoski, G. Merlo, E. Hassan, A. R. Field, L. Frassinetti, C. Giroud, J. C. Hillesheim, C. F. Maggi, C. Perez von Thun, C. M. Roach, S. Saarelma, D. Jarema, F. Jenko, and JET Contributors, "Microtearing modes as the source of magnetic fluctuations in the JET pedestal," *Nucl. Fusion* **61**(3), 036015 (2021).
- ⁹E. Hassan, D. R. Hatch, M. Halfmoon, M. Curie, M. Kotschenreuther, S. M. Mahajan, G. Merlo, R. J. Groebner, A. O. Nelson, and A. Diallo, "Identifying the microtearing modes in the pedestal of DIII-D H-modes using gyrokinetic simulations," *Nucl. Fusion* **62**, 026008 (2021).
- ¹⁰D. Told, F. Jenko, P. Xanthopoulos, L. D. Horton, and E. Wolfgrum, "Gyrokinetic microinstabilities in ASDEX upgrade edge plasmas," *Phys. Plasmas* **15**(10), 102306 (2008).

- ¹¹F. Jenko, D. Told, P. Xanthopoulos, F. Merz, and L. D. Horton, "Gyrokinetic turbulence under near-separatrix or nonaxisymmetric conditions," *Phys. Plasmas* **16**(5), 055901 (2009).
- ¹²D. R. Hatch, D. Told, F. Jenko, H. Doerk, M. G. Dunne, E. Wolfrum, E. Viezzer, ASDEX Upgrade Team, and M. J. Pueschel, "Gyrokinetic study of ASDEX Upgrade inter-ELM pedestal profile evolution," *Nucl. Fusion* **55**(6), 063028 (2015).
- ¹³D. R. Hatch, M. Kotschenreuther, S. Mahajan, P. Valanju, and X. Liu, "A gyrokinetic perspective on the JET-ILW pedestal," *Nucl. Fusion* **57**(3), 036020 (2017).
- ¹⁴D. R. Hatch, M. Kotschenreuther, S. M. Mahajan, G. Merlo, A. R. Field, C. Giroud, J. C. Hillesheim, C. F. Maggi, C. Perez von Thun, C. M. Roach, S. Saarelma, and JET Contributors, "Direct gyrokinetic comparison of pedestal transport in JET with carbon and ITER-like walls," *Nucl. Fusion* **59**(8), 086056 (2019).
- ¹⁵X. Liu, M. Kotschenreuther, D. R. Hatch, S. M. Mahajan, J. W. Hughes, and A. E. Hubbard, "Gyrokinetics investigations of an I-mode pedestal on Alcator C-Mod," *arXiv:2005.08924* (2020).
- ¹⁶B. Chapman-Opolopoiou, D. R. Hatch, A. R. Field, L. Frassinetti, J. C. Hillesheim, L. Horvath, C. F. Maggi, J. F. Parisi, C. M. Roach, S. Saarelma, J. Walker, and JET Contributors, "The role of ETG modes in JET-ILW pedestals with varying levels of power and fuelling," *Nucl. Fusion* (submitted).
- ¹⁷W. Guttenfelder, R. J. Groebner, J. M. Canik, B. A. Grierson, E. A. Belli, and J. Candy, "Testing predictions of electron scale turbulent pedestal transport in two DIII-D ELMy H-modes," *Nucl. Fusion* **61**(5), 056005 (2021).
- ¹⁸J. F. Parisi, F. I. Parra, C. M. Roach, C. Giroud, W. Dorland, D. R. Hatch, M. Barnes, J. C. Hillesheim, N. Aiba, J. Ball, and P. G. Ivanov, and Jet Contributors, "Toroidal and slab ETG instability dominance in the linear spectrum of JET-ILW pedestals," *Nucl. Fusion* **60**(12), 126045 (2020).
- ¹⁹F. Jenko, W. Dorland, M. Kotschenreuther, and B. N. Rogers, "Electron temperature gradient driven turbulence," *Phys. Plasmas* **7**, 1904 (2000).
- ²⁰W. Dorland, F. Jenko, M. Kotschenreuther, and B. N. Rogers, "Electron temperature gradient turbulence," *Phys. Rev. Lett.* **85**, 5579–5582 (2000).
- ²¹W. M. Nevins, J. Candy, S. Cowley, T. Dannert, A. Dimits, W. Dorland, C. Estrada-Mila, G. W. Hammett, F. Jenko, M. J. Pueschel, and D. E. Shumaker, "Characterizing electron temperature gradient turbulence via numerical simulation," *Phys. Plasmas* **13**(12), 122306 (2006).
- ²²E. Hassan, D. R. Hatch, W. Guttenfelder, Y. Chen, and S. Parker, "Gyrokinetic benchmark of the electron temperature-gradient instability in the pedestal region," *Phys. Plasmas* **28**(6), 062505 (2021).
- ²³L. Frassinetti, C. Perez von Thun, B. Chapman, A. Fil, J. C. Hillesheim, L. Horvath, G. T. A. Huijsmans, H. Nyström, V. Parail, S. Saarelma, G. Szepesi, B. Viola, R. Bianchetti Morales, M. Dunne, A. R. Field, J. Flanagan, J. M. Fontdecaba, D. Hatch, B. Lomanowski, C. F. Maggi, S. Menmuir, S. Pamela, C. M. Roach, E. Rachlew, E. R. Solano, and JET Contributors, "Role of the separatrix density in the pedestal performance in deuterium low triangularity JET-ILW plasmas and comparison with JET-C," *Nucl. Fusion* **61**(12), 126054 (2021).
- ²⁴K. Banker, D. Garrett, P. Bakkum, and S. Verch, *MongoDB in Action: Covers MongoDB Version 3.0* (Simon and Schuster, 2016).
- ²⁵M. Romanelli, R. Coelho, D. Coster, J. Ferreira, L. Fleury, S. Henderson, J. Hollocombe, F. Imbeaux, T. Jonsson, L. Kogan *et al.*, "Code integration, data verification, and models validation using the ITER integrated modeling and analysis system (IMAS) in EUROfusion," *Fusion Sci. Technol.* **76**(8), 894–900 (2020).
- ²⁶O. Meneghini, G. Snoep, B. C. Lyons, J. McClenaghan, C. S. Imai, B. Grierson, S. P. Smith, G. M. Staebler, P. B. Snyder, J. Candy, E. Belli, L. Lao, J. M. Park, J. Citrin, T. L. Cordemiglia, A. Tema, and S. Mordijck, "Neural-network accelerated coupled core-pedestal simulations with self-consistent transport of impurities and compatible with ITER IMAS," *Nucl. Fusion* **61**(2), 026006 (2020).
- ²⁷M. J. Pueschel, D. R. Hatch, M. Kotschenreuther, A. Ishizawa, and G. Merlo, "Multi-scale interactions of microtearing turbulence in the tokamak pedestal," *Nucl. Fusion* **60**(12), 124005 (2020).
- ²⁸G. M. Staebler, J. E. Kinsey, and R. E. Waltz, "Gyro-Landau fluid equations for trapped and passing particles," *Phys. Plasmas* **12**(10), 102508 (2005).
- ²⁹C. Bourdelle, X. Garbet, F. Imbeaux, A. Casati, N. Dubuit, R. Guirlet, and T. Parisot, "A new gyrokinetic quasilinear transport model applied to particle transport in tokamak plasmas," *Phys. Plasmas* **14**(11), 112501 (2007).
- ³⁰J. Citrin, C. Bourdelle, F. J. Casson, C. Angioni, N. Bonanomi, Y. Camenen, X. Garbet, L. Garzotti, T. Görler, O. Gürcan, F. Koechl, F. Imbeaux, O. Linder, K. van de Plassche, P. Strand, and G. Szepesi, "Tractable flux-driven temperature, density, and rotation profile evolution with the quasilinear gyrokinetic transport model QuaLiKiz," *Plasma Phys. Controlled Fusion* **59**(12), 124005 (2017).
- ³¹C. D. Stephens, X. Garbet, J. Citrin, C. Bourdelle, K. Lucas van de Plassche, and F. Jenko, "Quasilinear gyrokinetic theory: A derivation of QuaLiKiz," *J. Plasma Phys.* **87**(4), 905870409 (2021).
- ³²F. Merz and F. Jenko, "Nonlinear saturation of trapped electron modes via perpendicular particle diffusion," *Phys. Rev. Lett.* **100**, 035005 (2008).
- ³³T. Xie, M. J. Pueschel, and D. R. Hatch, "Quasilinear modeling of heat flux from microtearing turbulence," *Phys. Plasmas* **27**(8), 082306 (2020).
- ³⁴J. D. Callen, R. J. Groebner, T. H. Osborne, J. M. Canik, L. W. Owen, A. Y. Pankin, T. Rafiq, T. D. Rognlien, and W. M. Stacey, "Analysis of pedestal plasma transport," *Nucl. Fusion* **50**(6), 064004 (2010).
- ³⁵F. Jenko, "On the nature of ETG turbulence and cross-scale coupling," *J. Plasma Fusion Res.* **6**, 11–16 (2004).
- ³⁶R. Reksoatmodjo, S. Mordijck, J. W. Hughes, J. D. Lore, and X. Bonnin, "The role of edge fueling in determining the pedestal density in high neutral opacity Alcator C-Mod experiments," *Nucl. Mater. Energy* **27**, 100971 (2021).